Received: 4 August 2023 | Revised: 6 November 2023 | Accepted: 29 November 2023

DOI: 10.1002/nag.3705

RESEARCH ARTICLE

WILEY

Multiscale modeling of granular dynamics on flowslide triggering and runout

Ming Yang | **Giuseppe Buscarnera**

Department of Civil and Environmental Engineering, Northwestern University, Evanston, Illinois, USA

Correspondence
Giuseppe Buscarnera, Department of Civil and Environmental Engineering, Evanston, IL, USA.
Email: g-buscarnera@northwestern.edu

Funding information
National Science Foundation, Grant/Award Number: ICER-1854951; American Chemical Society Petroleum Research Fund

Abstract

A hierarchical multiscale modeling framework is proposed to simulate flowslide triggering and runout. It couples a system-scale sliding-consolidation model (SCM) resolving hydro-mechanical feedbacks within a flowslide with a local-scale solver based on the discrete element method (DEM) replicating the sand deformation response in the liquefied regime. This coupling allows for the simulation of a seamless transition from solid- to fluid-like behavior following liquefaction, which is controlled by the grain-scale dynamics. To investigate the role of grain-scale interactions, the DEM simulations replace the constitutive model within the SCM framework, enabling the capture of the emergent rate-dependent behavior of the sand during the inertial regime of motion. For this purpose, a novel algorithm is proposed to ensure the accurate passage of the strain rate from the global analysis to the local DEM solver under both quasi-static (pre-triggering) and dynamic (post-triggering) regimes of motion. Our findings demonstrate that the specifics of the coupling algorithm do not bear significant consequences to the triggering analysis, in that the grain-scale dynamics is negligible. By contrast, major differences between the results obtained with traditional algorithms and the proposed algorithm are found for the post-triggering stage. Specifically, the existing algorithms suffer from loss of convergence and require proper numerical treatment to capture the micro-inertial effects arising from the post-liquefaction particle agitation responsible for viscous-like effects that spontaneously regulate the flowslide velocity. These findings emphasize the important role of rate-dependent feedback for the analysis of natural hazards involving granular materials, especially for post-failure propagation analysis.

KEYWORDS
flowslide, granular dynamics, hydro-mechanical coupling, multiscale modeling

1 | INTRODUCTION

Loose granular soils initially deforming as solid materials can lose the ability of sustaining shear strength under external excitations, manifested in liquefaction instabilities, responsible for numerous catastrophic failures of geostructures such

as embankments, levees, and tailings dam.[1–4] This process involves three possible regimes of granular material under shearing depending on how particles interact,[5,6] including (1) quasi-static state with dominating frictional contacts under extremely slow shear strain rate, (2) intermediate granular flow governed by both frictional and collisional contacts under moderate shear strain rate, and (3) collisional state with dominating binary and uncorrelated collisional interactions under high shear strain rate. Modeling this process through continuum mechanics principles requires adequate representation of the complex rheological response of granular materials under different regimes, as well as of the transition across these regimes. Many attempts have been made to propose constitutive laws tackling the response of granular materials under each individual regime, based on, for example, soil mechanics for plastic flow, for example refs. [7–11], $\mu(I)$ rheology[12] for moderate granular flows, and kinetic theory[13] for rapid collisional flows. Although recently, promising attempts have been made to formulate unified modeling frameworks covering all such regimes,[14–17] this emerging class of continuum models still requires further evaluation.

In this context, multiscale modeling offers a viable alternative to bypass the complexities within multi-regime continuum modeling. Hierarchical multiscale modeling[18] is particularly effective as it involves the computational homogenization of local-scale quantities and the passage of information between global- and local-scale models. A notable example of this approach is the coupling of global continuum frameworks and local simulations based on the discrete element method (DEM). In such cases, global-scale models can be constructed using conventional finite element method (FEM) for small-strain problems[19–22] or material point method (MPM) and smoothed particle finite element method (SPFEM) for large-strain problems.[23–25] The local DEM solver replaces the constitutive model, in that it receives strain increments from the global model and returns the simulated stress tensor. While these techniques are increasingly used in numerous previous studies, it is important to note that the local DEM model is often operated with a rescaled loading rate. This approach is designed to maintain the local response within the quasi-static regime. While this logic is sound for the analysis of global-scale problems characterized by limited inertial processes (e.g., slow progressive failure involving the gradual development of a shear band[23,24]), it may introduce significant approximations when dealing with highly dynamic problems,[26] such as those involving flow-like behavior and consequent rate effects due to grain-scale inertial feedbacks.

This study aims to enhance hierarchical multiscale modeling frameworks by accounting for the rate-dependent behaviors that can spontaneously manifest in local DEM simulations. More generally, the primary objective of the study is to investigate the impact of grain-scale dynamics on the entire life cycle of flowslide triggering and runout. Given that the focus of the paper is on the accurate treatment of the passage of the strain rate from the global to the local scale, a reduced-order model is employed to address the hydromechanical couplings that engage sand deformation and pore pressure buildup. This framework is a member of the sliding-consolidation models (SCM) family.[27,28] It has been recently augmented to enable the versatile representation of the feedback between flowslide velocity and excess pore pressure dissipation, accommodating various constitutive relations for the deforming landslide material.[29] This choice offers the advantage of significantly reducing the computational costs involved in the continuum modeling of global problems through techniques for large deformation analyses (e.g., MPM, SPFEM). Simultaneously, it allows for an in-depth examination of the constitutive behavior that emerges from the chosen DEM solver, considering both flowslide triggering and runout. In the following sections, DEM simulations will be used to capture both the onset of liquefaction (the flowslide triggering stage) and the subsequent flow-like behavior (the flowslide runout stage). These simulations include the emergent rate effects arising from the inter-particle interactions resolved by the DEM. This approach enables us to bypass the specification of the deformation/flow regime of the granular material. Possible regime transitions are automatically captured by the DEM solver, as it conducts local analyses at deformation rates consistent with the global inertial behavior of the landslide system. As a result, the analyses are anticipated to highlight the role played by the rate of sand deformation at different stages of the flowslide process.

2 | NUMERICAL PLATFORM

2.1 | Sliding consolidation model

The balance equations governing the triggering and runout of a flowslide are here simulated at the system scale through the novel SCM framework proposed by Chen and Buscarnera.[29] The first proposition of an SCM dates back to the work by Hutchinson,[27] who examined the propagation behavior of a liquefied soil volume by modeling the competition between the frictional resistance at the base of the landslide and excess pore pressure dissipation. While the original SCM involved a one-way coupling between pore pressure and frictional strength, later developments of Iverson[28] allowed full coupling

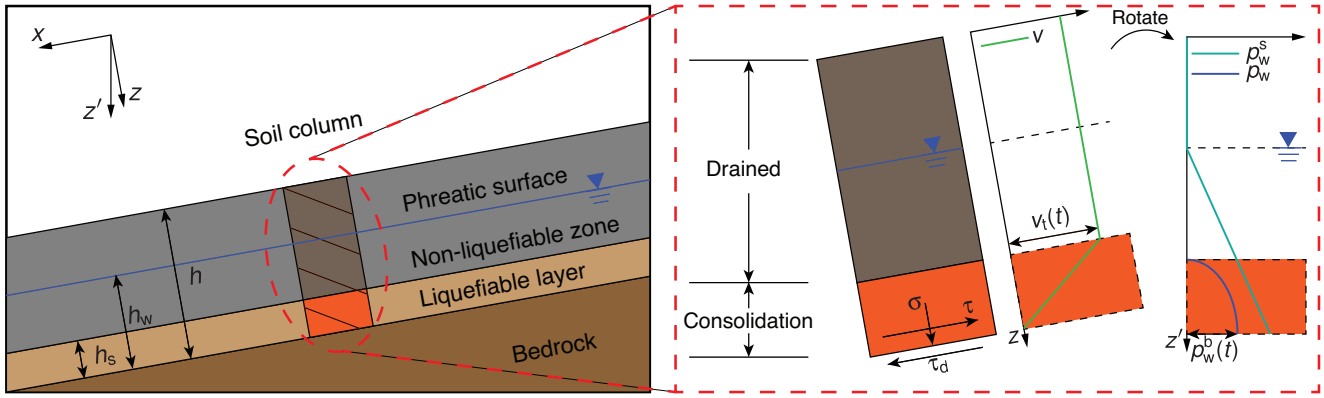

FIGURE 1 Idealization of a soil column with two assumptions in the liquefiable layer: (A) linear velocity profile along z direction and (B) parabolic distribution of excess pore pressure p_w along z' direction.

between sliding and consolidation. In this context, the work by Chen and Buscarnera further expands the scope of the application of this class of models by allowing a versatile selection of the constitutive behavior for the active zone of landslide deformation, inelastic effects in the rate of excess pore pressure dissipation, and a streamlined analysis of the entire cycle of pre-failure, triggering, and post-failure landslide dynamics.[29–31] Hereafter, the key features of the SCM model proposed by Chen and Buscarnera are briefly described.

For an infinite slope with phreatic surface parallel to the bedrock (Figure 1), the inelastic deformation is assumed to concentrate within a liquefiable layer of thickness h_s, while the stationary pore water pressure is governed by the phreatic surface (having elevation h_w from the base of the landslide). Two governing equations are established by considering downslope flow dynamics and vertical fluid diffusion:

$$ma = \tau_d - \tau, \tag{1}$$

$$\frac{k}{\gamma_w}\frac{\partial^2 p_w}{\partial z'^2} + \dot{\varepsilon} = 0. \tag{2}$$

Here m is the mass of the slope materials, a the slope movement acceleration, τ_d the driving shear stress, τ the resistance shear stress, k the hydraulic conductivity, γ_w the unit weight of water, p_w the excess pore pressure, and ε the normal strain perpendicular to the slope.

Assuming a linear distribution of the flow velocity v along the depth of the liquefiable layer with a zero basal velocity, we can determine the shear strain rate $\dot{\gamma}$ using the following equations:

$$\dot{\gamma} = -\frac{\partial v}{\partial z} = \frac{v_t}{h_s}, \tag{3}$$

$$v = v_t\left(1 - \frac{z}{h_s}\right), \tag{4}$$

where v_t is the flow velocity at the top surface of the liquefiable layer. Furthermore, Equation (2) can be simplified as:

$$\dot{\varepsilon} = \frac{2k}{\gamma_w(h_s\cos\theta)^2}p_w^b = \frac{2k}{\gamma_w(h_s\cos\theta)^2}(\sigma_d - \sigma), \tag{5}$$

assuming a parabolic distribution of excess pore pressure p along z' direction, given by:

$$p_w(z') = p_w^b\left[2\frac{z'}{h_s\cos\theta} - \left(\frac{z'}{h_s\cos\theta}\right)^2\right], \tag{6}$$

where p_w^b is the basal excess pore pressure, θ is the slope angle, σ_d is the driving normal stress to the slope, and σ is the resistance normal stress.

TABLE 1 DEM parameters.

Description	Value
Particle density, ρ	2650 kg/m^3
Young's modulus, E	2 GPa
Poisson's ratio, ν	0.25
Coefficient of restitution, ϵ	0.8
Tangential friction coefficient, μ	0.5
Rolling friction coefficient, μ_r	0.1

Abbreviation: DEM, discrete element method.

For simplicity, the following derivations neglect differences in soil density between the liquefiable and non-liquefiable portions of the slope profile. The mass of the moving slope is therefore expressed as a function of h_w,

$$m = \rho_{sat} h_w + \rho_d (h - h_w), \tag{7}$$

where ρ_d is the dry density of soil above the water table and ρ_{sat} is the saturated density of soil below the water table. In this study, we set $h_w = h_s$, which occupies 10% of the slope thickness h. The initial internal stress state (τ_0, σ_0) is determined to ensure equilibrium:

$$\tau_0 = [\rho_{sat} h_w + \rho_d (h - h_w)] g \sin\theta, \tag{8}$$

$$\sigma_0 = [(\rho_{sat} - \rho_w) h_w + \rho_d (h - h_w)] g \cos\theta. \tag{9}$$

Given the prescribed driving stress history (τ_d, σ_d), the two governing equations (1) and (5) with four unknown variables a, τ, ε, and σ require two additional constitutive relations to be solved. These constitutive relations are provided by the DEM to complete the analysis.

2.2 | Discrete element method

2.2.1 | Contact model

The local-scale simulations of sand deformation in this study utilize the open-source DEM program for particle dynamics simulation called LIGGGHTS.[32] The granular assembly consists of polydisperse spherical particles that interact through soft-contact laws. The contact interactions between particles are modeled using a Hertzian normal model and a history-dependent tangential model with a Coulomb friction cut-off. To simply account for effects of aspherical particle shape or surface roughness, the modified elastic-plastic spring dashpot model EPSD3[33] is employed to incorporate rolling resistance into spherical particles. The DEM parameters used in the simulations are listed in Table 1, which include particle density ρ, particle Young's modulus E, Poisson's ratio ν, coefficient of restitution ϵ, tangential friction coefficient μ, and rolling friction coefficient μ_r. In this study, a reduced value of E compared with around 70 GPa as reported by laboratory measurements[34,35] is adopted. This adjustment is made to diminish the excessive dilation observed within the DEM sample during the post-liquefaction period. Nevertheless, the chosen value for E remains sufficiently high to represent particles that are nearly undeformable, ensuring that the average normal deflection between particles is negligible compared to the particle size. The values of ν and ϵ closely align with those reported in previous measurements.[34,35] The high value of ϵ is selected to introduce a low viscous force for weak dissipation of kinetic energy during particle collisions. A common value of $\mu = 0.5$ is used in the shearing stage, as found in the literature [36], to ensure the DEM sample exhibits a reasonable critical state friction angle. The rolling friction coefficient μ_r is set to a small nonzero value to enhance dissipation while sliding friction remains the main contributing factor. LIGGGHTS adopts an explicit velocity-Verlet time-stepping scheme to update the positions, velocities, and angular velocities of the spherical particles. The time step size Δt_L = 5e-7 s is chosen to be less than 5% of the Rayleigh-wave propagation time scale and Hertz contact time scale, ensuring sufficient accuracy in the numerical simulations.

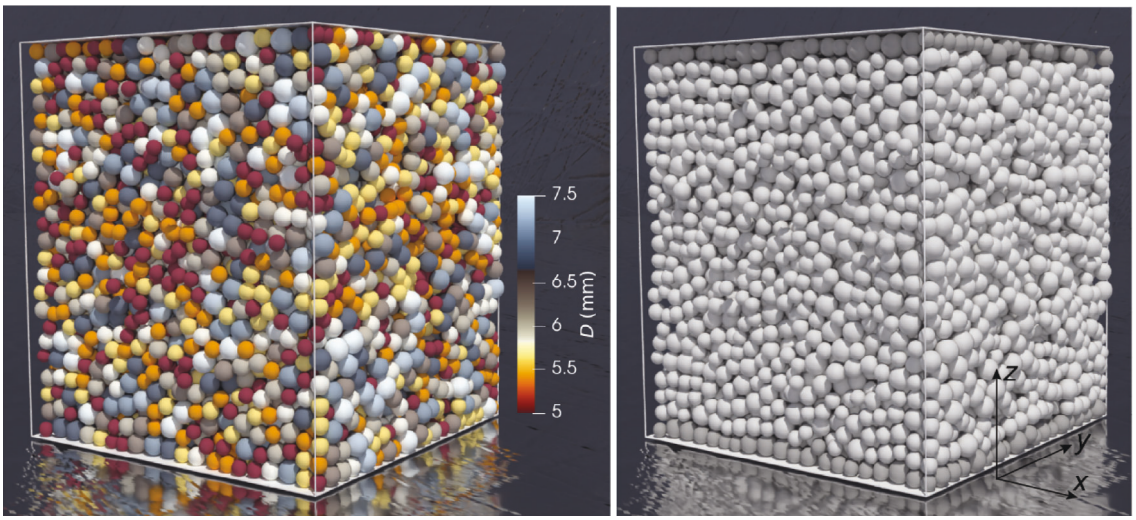

(A) (B)

FIGURE 2 Illustration of particle arrangement and boundary conditions for a DEM sample composed of 8800 particles: (A) at the end of sample preparation; (B) during shearing. The dark particles are glued to the top and bottom walls of the simulation cell. DEM, discrete element method.

In this study, the DEM samples are constructed using 8800 spheres with low polydispersity, where $D_{max}/D_{min} = 1.5$ and $D_{min} = 5$ mm, with D_{max} and D_{min} representing the maximum and minimum particle diameters, respectively. The particle sizes between D_{min} and D_{max} follow a uniform distribution of particle volumes. These particles are randomly generated and placed on a three-dimensional (3D) sparse lattice of $20 \times 20 \times 22$ to ensure that there is no overlap between particles. This 3D lattice is contained in a rectangular cell, where all six sides of the cell act as rigid walls. To achieve the desired stress state $\boldsymbol{\sigma}_0$, which should be compatible with the initial internal stress state (τ_0, σ_0) provided by the SCM, the sample is compressed by translating the six sides of the cell. In the DEM simulations, we consider the stress components σ_{zx} (or σ_{xz}) and σ_{zz} of the stress tensor $\boldsymbol{\sigma}$ as the shear stress τ and normal stress σ, respectively, in the SCM. Therefore, we set $\sigma_{zx0} = \tau_0$ and $\sigma_{zz0} = \sigma_0$ to match the initial stress state. For simplicity, the other normal stress components of $\boldsymbol{\sigma}_0$, including σ_{xx0} and σ_{yy0}, are set equal to σ_0, while the other shear stress components are set to zero.

The DEM sample is prepared following a four-stage sample preparation process[37,38]: (1) using a small tangential friction coefficient $\mu = \mu_I$ and compressing the sparse cell by moving the six rigid walls at a constant small velocity until the void ratio e reaches 1.2; (2) setting the velocities of all six walls to zero and using a servo-control algorithm to densify the sample isotropically to the target mean stress $p = 0.1\sigma_0$ with the same μ_I; (3) replacing the four lateral sides with periodic boundaries, increasing the target mean stress to $0.2\sigma_0$, and continuing isotropic compression with the same μ_I; (4) modifying $\mu = 0.5$ for further compressing the sample anisotropically to the final target stress state where three normal stresses reach σ_0 and shear stress σ_{zx} equals τ_0. It should be noted that the choice of μ_I determines the sample density. In this study, we use a relatively high value of μ_I to prepare loose granular packings. Figure 2A shows an example of a sample prepared using the above procedure. The sample is placed in the bi-periodic simulation cell, where the top and bottom sides are rigid walls, and the four lateral sides are periodic boundaries.

During simple shearing, the four lateral sides are fixed to constrain lateral normal strains. The bottom wall is also fixed, and only the top wall is allowed to move horizontally or vertically to induce shear or volumetric strain, respectively. To reduce possible slippage between the walls and the sample, one layer of particles is glued to the top and bottom walls. These glued particles are represented by the dark spheres in Figure 2B. Figure 3 presents the macroscopic response of simulated undrained simple shear tests on four DEM samples under a small constant shear strain rate $\dot{\gamma} \simeq 0.06\ s^{-1}$. Undrained shearing is achieved by maintaining a fixed sample height throughout the simulation, thereby preserving a constant volume. The use of the constant $\dot{\gamma}$ serves to ensure quasi-static loading conditions prior to liquefaction. We verify this by monitoring the dimensionless inertial number $I = \dot{\gamma}\bar{D}\sqrt{\rho/p}$, where $\bar{D}$ the average particle diameter, ρ particle density, and p the mean stress. Shear deformation is considered to be nearly quasi-static if $I \ll 1$ and typically the threshold is assumed to coincide with 1e-3. However, Figure 3C suggests that I can surpass this threshold due to unstable deformation and a sudden decrease in p. This behavior is an inherent characteristic of liquefaction and remains unaltered by variations in the

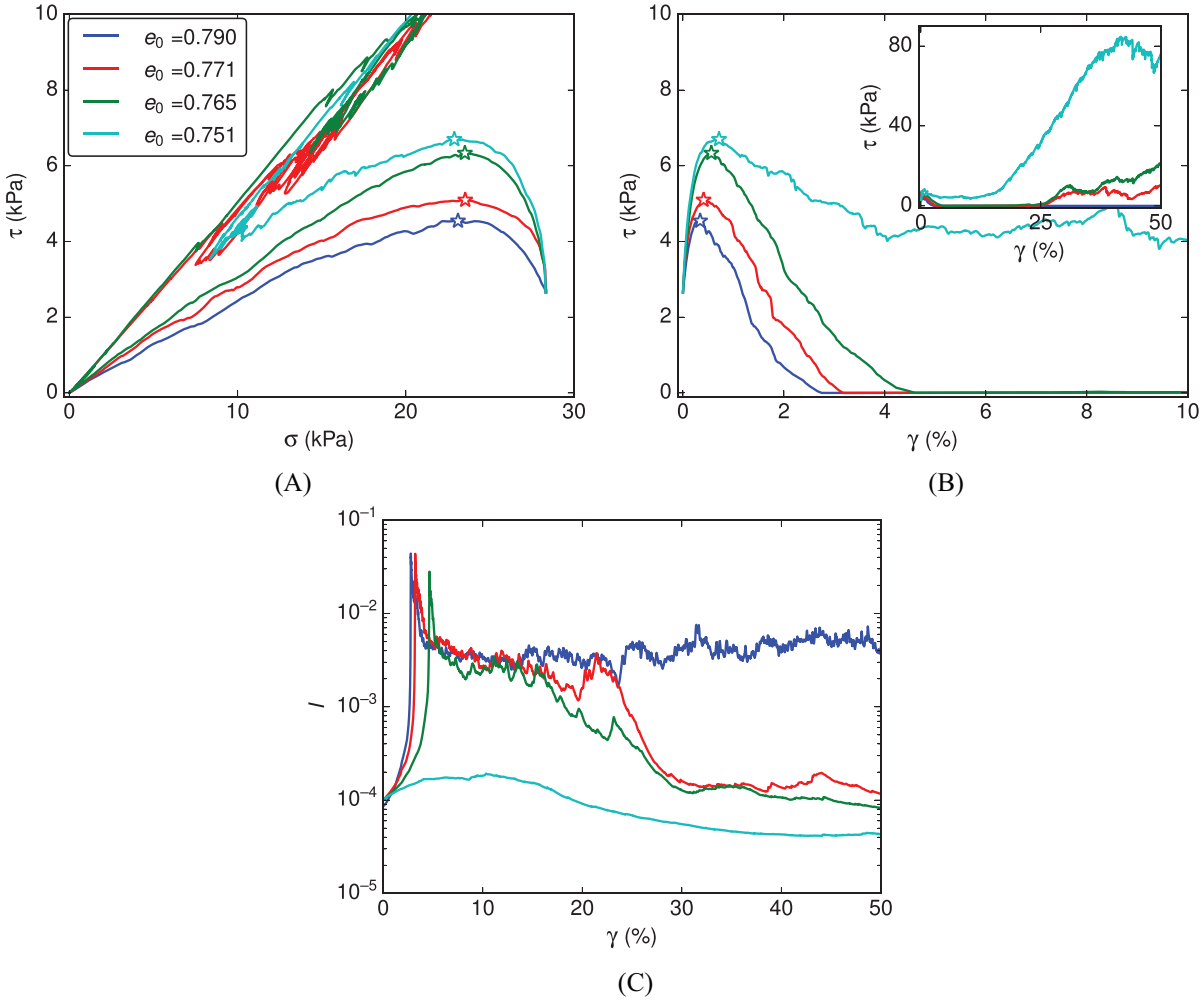

FIGURE 3 DEM simulated macroscopic results of constant-volume (undrained) simple shear tests on loose packings: (A) stress path, (B) stress-strain response, and (C) evolution of inertial number I. DEM, discrete element method.

loading rate. Note that p never reaches zero as otherwise I would diverge. The four DEM samples in Figure 3 exhibit local peak shear stress in undrained simple shear tests, followed by massive decrease of normal stress and noticeable generation of shear strain, a phenomenon named undrained instability widely observed in loose saturated sands. After instability, the sample with $e_0 = 0.790$ keep contracting and falls into full liquefaction with negligible effective stress, losing shear stress completely while the one with $e_0 = 0.751$ contracts first and then dilates, regaining significant shear strength. The two samples in between fall into complete liquefaction first and then regain shear strength when shear strain develops more than 25%, as shown in the inset window of Figure 3B.

2.2.2 | Homogenization of the material response

Before conducting multiscale analyses, it is necessary to determine an average stress tensor that appropriately captures the influence of loading rate on the response of the DEM sample. The average stress tensor $\langle \boldsymbol{\sigma}^{\mathcal{B}} \rangle$ for the selected region $\mathcal{B}$ of the granular system can be obtained through a volume-based homogenization of the particle average stress tensor $\langle \boldsymbol{\sigma}^{p} \rangle$[39,40]:

$$\langle \boldsymbol{\sigma}^{\mathcal{B}} \rangle = \frac{1}{V^{\mathcal{B}}} \sum_{p \in \mathcal{B}} V^{p,\mathcal{B}} \langle \boldsymbol{\sigma}^{p} \rangle. \tag{10}$$

Here, $V^{p,\mathcal{B}}$ represents the intersection volume of particle p with the region $\mathcal{B}$. If particle p is fully contained within the region $\mathcal{B}$, $V^{p,\mathcal{B}}$ is equal to the volume of particle p denoted as V^p.

The particle average stress tensor $\langle \boldsymbol{\sigma}^p \rangle$ that incorporates inertial effects is derived based on the approach proposed by Nicot et al.,[41] which satisfies the linear momentum balance of particle p:

$$\langle \boldsymbol{\sigma}^p \rangle = \frac{1}{V^p} \sum_{c \in C^p} \boldsymbol{r}^{c,p} \otimes \boldsymbol{f}^{c,p} - \frac{1}{V^p} \boldsymbol{\chi} \cdot \left[(\dot{\boldsymbol{\omega}}^p \cdot \boldsymbol{\epsilon}) + \boldsymbol{\omega}^p \otimes \boldsymbol{\omega}^p - ||\boldsymbol{\omega}^p||^2 \mathbf{I} \right]. \tag{11}$$

The first term on the right hand side (RHS) corresponds to the contact formulation in quasi-static regime, while the second term, involving rotational velocities and accelerations of particle p, accounts for inertial mechanisms. In the first term, C^p represents the contact set of particle p, $\boldsymbol{r}^{c,p} = \boldsymbol{r}^c - \boldsymbol{r}^p$ connects the contact point c with the center of particle p, and $\boldsymbol{f}^{c,p}$ is the contact force applied on particle p at the contact point c. In the second term, $\boldsymbol{\chi} = \int_{V^p} \rho \boldsymbol{r} \otimes \boldsymbol{r} \mathrm{d}V$, where $\boldsymbol{r} = \boldsymbol{x} - \boldsymbol{r}_c$ and $\boldsymbol{x}$ is the position vector. $\boldsymbol{\chi}$ is known as the inertia matrix, different from the moment of inertia in the diagonal components. $\boldsymbol{\epsilon}$ denotes the Levi-Civita symbol, $\boldsymbol{\omega}^p$ is the particle's rotational velocity vector, and $\mathbf{I}$ represents the second-order identity tensor.

Assume that all particles are contained within the region $\mathcal{B}$, implying $V^{p,\mathcal{B}} = V^p$ in Equation (10). Under quasi-static loading conditions, where the unbalanced force/torque for each particle is negligible, Equation (10) can be combined with Equation (11), omitting the second RHS term, resulting in Bagi's stress tensor formulation[42]:

$$\langle \boldsymbol{\sigma} \rangle_{\mathrm{B}} = \frac{1}{V^{\mathcal{B}}} \left[\sum_{c \in \mathcal{I}} \boldsymbol{l}^c \otimes \boldsymbol{f}^c + \sum_{e \in \mathcal{E}} \boldsymbol{l}^e \otimes \boldsymbol{f}^e \right]. \tag{12}$$

Here $\mathcal{I}$ represents the set of interior contacts, $\boldsymbol{l}^c$ is the branch vector connecting the centers of two particles in contact, $\mathcal{E}$ denotes the set of exterior contacts (contact point on the boundary of $\mathcal{B}$), and $\boldsymbol{l}^e$ is the vector connecting the particle center to the contact point.[40] For a granular system subjected to dynamic loading, we can substitute Equation (11) into Equation (10) to obtain the stress tensor formulation proposed by Nicot et al.[41]:

$$\langle \boldsymbol{\sigma} \rangle_{\mathrm{N}} = \langle \boldsymbol{\sigma} \rangle_{\mathrm{B}} - \frac{1}{V^{\mathcal{B}}} \sum_{p \in \mathcal{B}} \boldsymbol{\chi} \cdot \left[(\dot{\boldsymbol{\omega}}^p \cdot \boldsymbol{\epsilon}) + \boldsymbol{\omega}^p \otimes \boldsymbol{\omega}^p - ||\boldsymbol{\omega}^p||^2 \mathbf{I} \right]. \tag{13}$$

It should be noted that Equation (13) slightly differs from the equation presented by Nicot et al.,[41] as the first RHS term of Equation (13) is expressed through the Love-Weber stress tensor formula.[43,44] This formulation does not distinguish between interior and exterior contacts. The Love-Weber formula is applicable in cases where no exterior contacts exist, such as a cubic DEM sample with all six sides as periodic boundaries. However, it is known that small approximations in the contributions of peripheral particles can lead to significant and inaccurate calculation of the homogenized stress tensor.[45,46]

Figure 4 illustrates the results of a constant-volume simple shear test on a loosely isotropically consolidated DEM sample, subjected to two different loading rates characterized by the dimensionless inertial number I. The cases with I = 1e-4 and 2e-2 represent the quasi-static and dynamic loading conditions, respectively. Clearly, the macroscopic behaviors of both cases are significantly different due to the distinct loading rates. In each case, both stress tensor formulations, given by Equations (12) and (13), are employed to analyze the stress evolution. Surprisingly, regardless of the loading rate, the stress paths obtained using Bagi's and Nicot's stress tensor formulations completely overlap, suggesting a negligible contribution from the second RHS term of Equation (13). Within the range of I considered in this study, the rate effect on the macroscopic stress path is primarily captured by the first RHS term of Equation (13), which accounts for the persistent contact network, rather than the second RHS term that directly incorporates the inertial effects of particles.

It is important to highlight that Equation (13) does not account for the kinetic or streaming contribution related to the fluctuating velocities $\tilde{\boldsymbol{v}}^p$ of the particles. This contribution is expressed by the kinetic stress tensor[47,48]:

$$\langle \boldsymbol{\sigma} \rangle_k = \frac{1}{V^{\mathcal{B}}} \sum_{p \in \mathcal{B}} m^p \tilde{\boldsymbol{v}}^p \otimes \tilde{\boldsymbol{v}}^p, \tag{14}$$

where m^p represents the mass of particle p. We analyzed the effect of $\langle \boldsymbol{\sigma} \rangle_k$ in the subsequent multiscale modeling simulations and observed negligible contributions (less than 0.5%) to the total stress tensor $\langle \boldsymbol{\sigma} \rangle_{\mathrm{N}} + \langle \boldsymbol{\sigma} \rangle_k$. Consequently, one can use $\langle \boldsymbol{\sigma} \rangle_{\mathrm{B}}$, $\langle \boldsymbol{\sigma} \rangle_{\mathrm{N}}$, or $\langle \boldsymbol{\sigma} \rangle_{\mathrm{N}} + \langle \boldsymbol{\sigma} \rangle_k$ for the following multiscale modeling analyses. In this study, we adopt $\langle \boldsymbol{\sigma} \rangle_{\mathrm{N}}$.

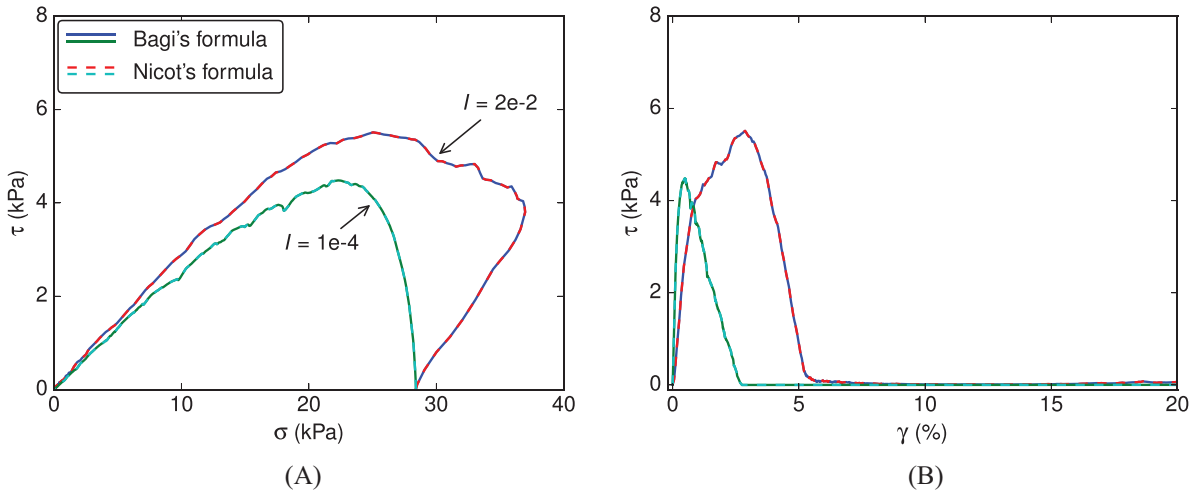

FIGURE 4 DEM simulation results of constant-volume simple shear tests under different loading rates quantified by the inertial number I: (A) stress path and (B) stress-strain response. DEM, discrete element method.

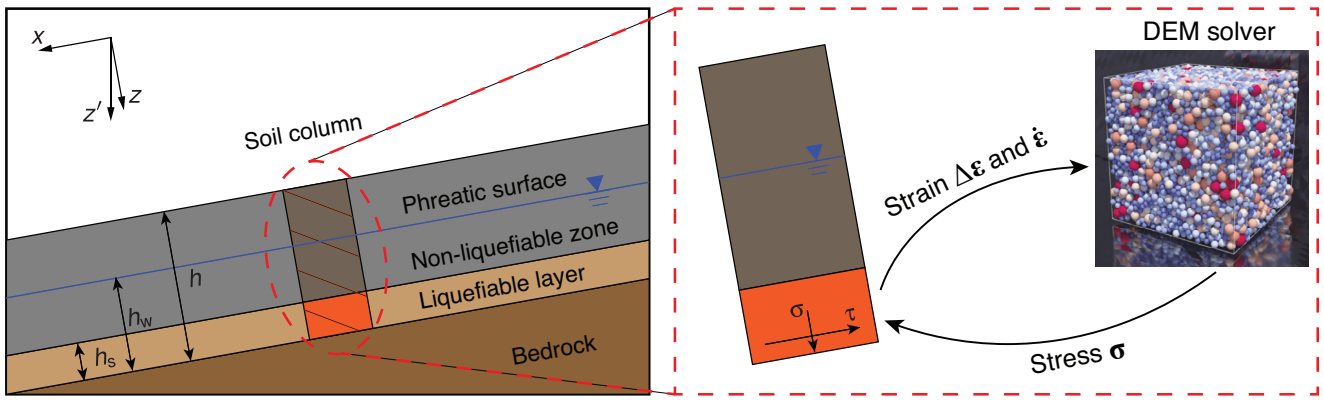

FIGURE 5 Illustration of the hierarchical multiscale coupling scheme of SCM and DEM. DEM, discrete element method; SCM, sliding-consolidation model.

2.3 | Hierarchical coupling between SCM and DEM

Figure 5 presents a schematic of the hierarchical multiscale model that couples the global-scale SCM with the local-scale DEM solver. In this model, the DEM sample functions as the constitutive model, deforming in response to the received strain increment and strain rate from the SCM, and providing the computed stress tensor back to the global-scale model. We adopt an explicit time integration scheme that combines the central difference method and forward Euler method for integrating the equations of sliding dynamics and fluid diffusion, respectively. Please refer to Algorithm 1 for more detailed information on the integration procedure. Furthermore, this algorithm is designed to support MPI parallel computing, with one CPU dedicated to global-scale model integration and all the CPUs assigned to the local-scale DEM calculations.

One of the main challenges in the multiscale coupling is establishing the relation between the global-scale strain $\boldsymbol{\varepsilon}_{\mathrm{G}}$ and the local-scale strain $\boldsymbol{\varepsilon}_{\mathrm{L}}$. Traditionally, many studies, for example refs. [20, 22, 49], have assumed that the global-scale strain increment $\Delta\boldsymbol{\varepsilon}_{\mathrm{G}}$ is equal to the local-scale strain increment $\Delta\boldsymbol{\varepsilon}_{\mathrm{L}}$, that is, $\Delta\boldsymbol{\varepsilon}_{\mathrm{G}} = \Delta\boldsymbol{\varepsilon}_{\mathrm{L}}$. However, the relation between the global level strain rate $\dot{\boldsymbol{\varepsilon}}_{\mathrm{G}}$ and the local level strain rate $\dot{\boldsymbol{\varepsilon}}_{\mathrm{L}}$ remains unclear. Previous studies have often neglected this relation and instead rescaled the local strain rate to lower values in order to achieve quasi-static deformation of the DEM sample, thus assuming a rate-independent material model. For instance, a scalar value can be defined as the upper bound strain rate $\dot{\varepsilon}_{\mathrm{L}}^{\mathrm{U}}$ applied to DEM sample, and the number of DEM running steps n_{step} and the local-scale strain rate $\dot{\boldsymbol{\varepsilon}}_{\mathrm{L}}$ can be determined as follows:

$$n_{\mathrm{step}} = \left\lfloor \|\Delta\boldsymbol{\varepsilon}_{\mathrm{G}}\| / \left(\dot{\varepsilon}_{\mathrm{L}}^{\mathrm{U}} \Delta t_{\mathrm{L}}\right) \right\rfloor + 1, \tag{15a}$$

ALGORITHM 1 Explicit time integration scheme for hierarchical coupling of SCM/DEM multiscale approach.

Initialize $x^0, v^0, \varepsilon^0, \Delta t, t = 0$
Compute $a^0 = \left(\tau_d^0 - \tau^0\right)/m, v\left(\frac{1}{2}\Delta t\right) = v^0 + \frac{1}{2}\Delta t a^0$
while $t < t_f$ **do**
  Displacement: $x^{t+\Delta t} = x^t + \Delta t v^{t+\frac{1}{2}\Delta t}, \varepsilon^{t+\Delta t} = \varepsilon^t + \Delta t \frac{2k}{\gamma_w (h_s \cos\theta)^2}\left(\sigma_d^t - \sigma^t\right)$
  Strain increment: $\Delta\gamma = \Delta x/h_s, \Delta\varepsilon = \varepsilon^{t+\Delta t} - \varepsilon^t, \Delta x = x^{t+\Delta t} - x(t)$
  Convert $(\Delta\gamma, \Delta\varepsilon)$ to (n_{step}, v_{xz}, v_z) used for DEM simulations
  Run n_{step} DEM steps using v_{xz} and v_z to shear RVE and return $\Delta\tau$ and $\Delta\sigma$
  Compute $\tau^{t+\Delta t} = \tau^t + \Delta\tau, \sigma^{t+\Delta t} = \sigma^t + \Delta\sigma$
  Compute $a^{t+\Delta t} = \frac{1}{m}\left(\tau_d^{t+\Delta t} - \tau^{t+\Delta t}\right)$
  Compute $v^{t+\frac{3}{2}\Delta t} = v^{t+\frac{1}{2}\Delta t} + \Delta t a^{t+\Delta t}$
  $t \leftarrow t + \Delta t$
end while

$$t_{DEM} = n_{step}\Delta t_L, \tag{15b}$$

$$\dot{\boldsymbol{\varepsilon}}_L = \Delta\boldsymbol{\varepsilon}_G / t_{DEM}, \tag{15c}$$

where Δt_L represents the DEM time step, t_{DEM} refers to the local-scale simulation time, $\|\cdot\|$ represents the norm of a vector, $\lfloor\cdot\rfloor$ represents the integer part of a number, and the 1 in Equation (15a) avoids a zero t_{DEM}, otherwise causing an issue in Equation (15c). Equations (15) can be interpreted as follows:

$$\|\dot{\boldsymbol{\varepsilon}}_L\| \simeq \dot{\varepsilon}_L^U, \text{ if } \left\lfloor \|\Delta\boldsymbol{\varepsilon}_G\| / \left(\dot{\varepsilon}_L^U \Delta t_L\right)\right\rfloor + 1 \simeq \|\Delta\boldsymbol{\varepsilon}_G\| / \left(\dot{\varepsilon}_L^U \Delta t_L\right), \tag{16a}$$

$$\|\dot{\boldsymbol{\varepsilon}}_L\| \simeq \|\Delta\boldsymbol{\varepsilon}_G\|/\Delta t_L \ll \dot{\varepsilon}_L^U, \text{ if } \left\lfloor \|\Delta\boldsymbol{\varepsilon}_G\| / \left(\dot{\varepsilon}_L^U \Delta t_L\right)\right\rfloor \ll 1. \tag{16b}$$

Equation (16a) works as expected. However, Equation (16b) indicates a significant discrepancy between the specified strain rate $\dot{\varepsilon}_L^U$ and the rate $\dot{\boldsymbol{\varepsilon}}_L$ applied to the DEM sample. This discrepancy does not matter in cases where changes in strain rate do not significantly affect the response, such as quasi-static shearing. However, if the loading rate effect is significant, Equation (16b) can cause numerical convergence issues, meaning that the simulation results will change with the global level time step Δt_G. This is because smaller Δt_G will activate Equation (16b) more frequently given the same global-scale strain rate $\dot{\boldsymbol{\varepsilon}}_G$. For instance, consider a simulation with Δt_G such that $n_{step} = 10$ at a certain stage, implying $\lfloor \|\Delta\boldsymbol{\varepsilon}_G\|/(\dot{\varepsilon}_L^U \Delta t_L)\rfloor = 9$. The local DEM solver will run with $\|\dot{\boldsymbol{\varepsilon}}_L\| \simeq \dot{\varepsilon}_L^U$. If we rerun the simulation using one hundredth of Δt_G and assume negligible changes in $\dot{\boldsymbol{\varepsilon}}_G$ within Δt_G, then at each global step equal to $0.01\Delta t_G$, $n_{step} = 1$ since $\lfloor 0.01\|\Delta\boldsymbol{\varepsilon}_G\|/(\dot{\varepsilon}_L^U \Delta t_L)\rfloor = 0$, and $\|\dot{\boldsymbol{\varepsilon}}_L\| \simeq 0.1\dot{\varepsilon}_L^U$. Despite having $\Delta\boldsymbol{\varepsilon}_G = \Delta\boldsymbol{\varepsilon}_L$, the latter simulation with $0.01\Delta t_G$ will noticeably diminish the rate effect.

Figure 6 demonstrates the convergence of multiscale simulations that couple SCM and DEM. The strain increment $\Delta\boldsymbol{\varepsilon}_G$ from SCM is applied to a loose DEM sample with the strain rate derived from I. Pure DEM simulation results, including stress path and stress-strain response, are included for comparison. Ideally, one would expect perfect agreement between the SCM/DEM multiscale modeling and pure DEM simulations when using the same I. This agreement holds for low I, as shown in Figures 6A,C. The choice of Δt_G has negligible effects on the simulations, including the sliding velocity evolution in Figure 6E with low I, unless Δt_G is very small due to explicit integration. However, these agreements and convergence with reducing Δt_G do not apply to the multiscale simulation results for high I = 1e-2, as shown in Figures 6B,D,F. Interestingly, even better agreement is observed between the multiscale modeling results using large Δt_G = 1e-3 s and the pure DEM data, which can be attributed to Equation (16b) being activated less frequently, thereby preserving the rate effect. As Δt_G is reduced to 1e-6 s, the multiscale simulation results become more similar to those obtained under quasi-static loading, deviating significantly from the pure DEM data with I = 1e-2 at the beginning of loading. Furthermore, the computed sliding velocity evolution is affected by the choice of Δt_G.

Considering the limitations of Equation (16b) in handling high loading rates on the local-scale DEM, we can propose two numerical strategies to avoid Equation (16b) and ensure that $\|\dot{\boldsymbol{\varepsilon}}_L\| \simeq \dot{\varepsilon}_L^U$ at all times:

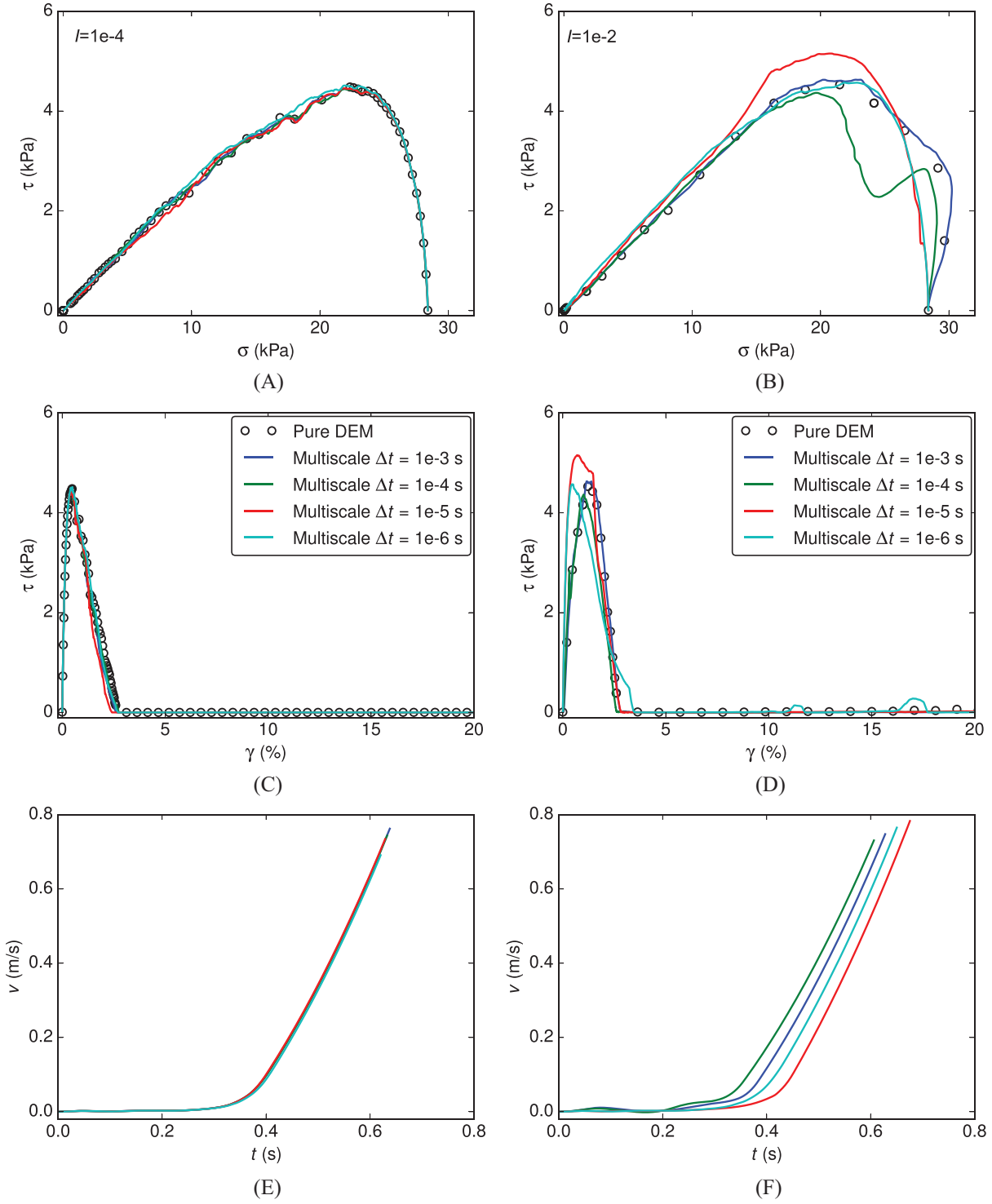

FIGURE 6 Convergence of multiscale modeling results coupling SCM with RI-DEM and comparison with pure DEM simulation response: (A) stress path, (C) stress-strain relation, and (E) sliding velocity evolution for loading rate of I = 1e-4; (B) stress path, (D) stress-strain relation, and (F) sliding velocity evolution for loading rate of I = 1e-2. DEM, discrete element method; RI-DEM, rate-independent DEM; SCM, sliding-consolidation model.

1. If the DEM time step Δt_{L} is adjustable, we can continuously reduce Δt_{L} so that the first RHS term in Equation (15a) always return an integer value greater than 1. This approach ensures that Equation (16a) is activated instead of Equation (16b). For example, we can define a default DEM time step $\Delta t_{\mathrm{L}}^{\mathrm{U}}$ as an upper bound of Δt_{L}:

$$t_{\mathrm{DEM}} = \Delta \varepsilon_{\mathrm{G}} / \dot{\varepsilon}_{\mathrm{L}}^{\mathrm{U}}, \tag{17a}$$

$$n_{\text{step}} = \left\lfloor t_{\text{DEM}}/\Delta t_{\text{L}}^{\text{U}} \right\rfloor + 1, \tag{17b}$$

$$\Delta t_{\text{L}} = t_{\text{DEM}}/n_{\text{step}}. \tag{17c}$$

In this case, we ensure that $\Delta t_{\text{L}} \lesssim \min\{\Delta t_{\text{L}}^{\text{U}}, \|\Delta \boldsymbol{\varepsilon}_{\text{G}}\|/\dot{\varepsilon}_{\text{L}}^{\text{U}}\}$. The validity of Equation (17) relies on the assumption that the effect of DEM time step Δt_{L} on the DEM simulation results is negligible unless it becomes sufficiently small, regardless of the loading rate.

2. If the DEM time step Δt_{L} can not be adjusted or varying it is impractical, an alternative approach is to introduce an additional term $\boldsymbol{\varepsilon}_{\text{L}}^{\text{accum}}$ that accumulates $\Delta \boldsymbol{\varepsilon}_{\text{G}}$ until the condition

$$n_{\text{step}} = \left\lfloor \|\boldsymbol{\varepsilon}_{\text{L}}^{\text{accum}}/\left(\dot{\varepsilon}_{\text{L}}^{\text{U}} \Delta t_{\text{L}}\right)\| \right\rfloor + 1 \geq n_{\text{step}}^{\text{accum}} \tag{18}$$

is satisfied, where $n_{\text{step}}^{\text{accum}}$ is a user-defined integer greater than 1. During the accumulation of small Δt_{G} increments, the local DEM solver is not executed, and only the global-scale integration continues without updating DEM-related quantities, such as stresses and void ratio (i.e., $\Delta\tau = 0$ and $\Delta\sigma = 0$ in step 7 of Algorithm 1). Once $\boldsymbol{\varepsilon}_{\text{L}}^{\text{accum}}$ reaches a sufficient magnitude to satisfy Equation (18), the local DEM solver runs for n_{step} steps, followed by global-scale integration of SCM. Afterwards, $\boldsymbol{\varepsilon}_{\text{L}}^{\text{accum}}$ is reset to zero. It is important to note that setting $n_{\text{step}}^{\text{accum}} = 1$ implies that the algorithm reverts to operating according to Equations (16), essentially recovering the standard algorithm discussed previously as a special case.

Due to the limited flexibility of the LIGGGHTS configuration in changing DEM time step Δt_{L}, we can only implement the second numerical strategy discussed earlier. Therefore, we rerun the multiscale simulations presented in Figure 6 using Equation (18) with $n_{\text{step}}^{\text{accum}} = 10$. The results of these simulations are shown in Figure 7. Notably, this approach does not affect the simulated response of the local DEM sample under quasi-static loading, ensuring that the results remain consistent. However, it guarantees convergence and maintains good agreement with pure DEM simulation results when dealing with high loading rates. We also verify that further increasing the value of $n_{\text{step}}^{\text{accum}}$ does not noticeably alter the simulation results.

While the procedures mentioned earlier address the numerical challenges associated with shearing the local DEM sample at a high strain rate, they do not entirely eliminate the issue of the mismatch between $\dot{\boldsymbol{\varepsilon}}_{\text{G}}$ and $\dot{\boldsymbol{\varepsilon}}_{\text{L}}$, which involves the temporal scales of both global and local scales. In this study, we make the simplifying assumption that $\dot{\boldsymbol{\varepsilon}}_{\text{G}}$ and $\dot{\boldsymbol{\varepsilon}}_{\text{L}}$ are equal, that is, $\dot{\boldsymbol{\varepsilon}}_{\text{L}} = \dot{\boldsymbol{\varepsilon}}_{\text{G}}$. This assumption serves as an additional constraint for the information exchange between scales, along with $\Delta \boldsymbol{\varepsilon}_{\text{L}} = \Delta \boldsymbol{\varepsilon}_{\text{G}}$. At each global time step Δt_{G}, the computed $\dot{\boldsymbol{\varepsilon}}_{\text{G}}$ corresponds to $\dot{\varepsilon}_{\text{L}}^{\text{U}}$ of Equation (18), which determines the rate at which the local DEM sample is sheared. We refer to this multiscale modeling scheme as SCM/RD-DEM, where RD stands for rate-dependent, indicating the incorporation of the specified $\dot{\varepsilon}_{\text{L}}^{\text{U}}$ and $\dot{\boldsymbol{\varepsilon}}_{\text{G}}$. Additionally, we have the conventional multiscale modeling scheme, SCM/RI-DEM with RI representing rate-independent, where $\dot{\varepsilon}_{\text{L}}^{\text{U}}$ is set to a small value to ensure quasi-static loading and is therefore detached from $\dot{\boldsymbol{\varepsilon}}_{\text{G}}$. By comparing the simulation results obtained from SCM/RD-DEM and SCM/RI-DEM, we can assess the effect of strain rate on flowslide triggering and runout.

3 | SIMULATION RESULTS

3.1 | Flowslide triggering

To investigate the influence of grain-scale interaction dynamics on flowslide triggering, we apply a shear load to the sloping ground at a constant rate of $\dot{\tau}_{\text{d}} = 1\text{e}3$ kPa/min using both the RI-DEM and RD-DEM schemes. The properties of the sloping ground are listed in Table 2. Figure 8 compares the multiscale modeling results obtained from SCM/RD-DEM and SCM/RI-DEM for the sloping ground. In the SCM/RI-DEM simulation, the DEM sample is sheared with an inertial number $I = 1\text{e}{-4}$, as depicted by the solid blue line in Figure 8D, where the dashed curves represent the computed inertial number using the global-scale strain rate $\dot{\boldsymbol{\varepsilon}}_{\text{G}}$. Before the shear stress τ reaches its peak, indicated by the asterisk marker, both simulations exhibit a very similar response, characterized by low sliding velocity and inertial number within the range

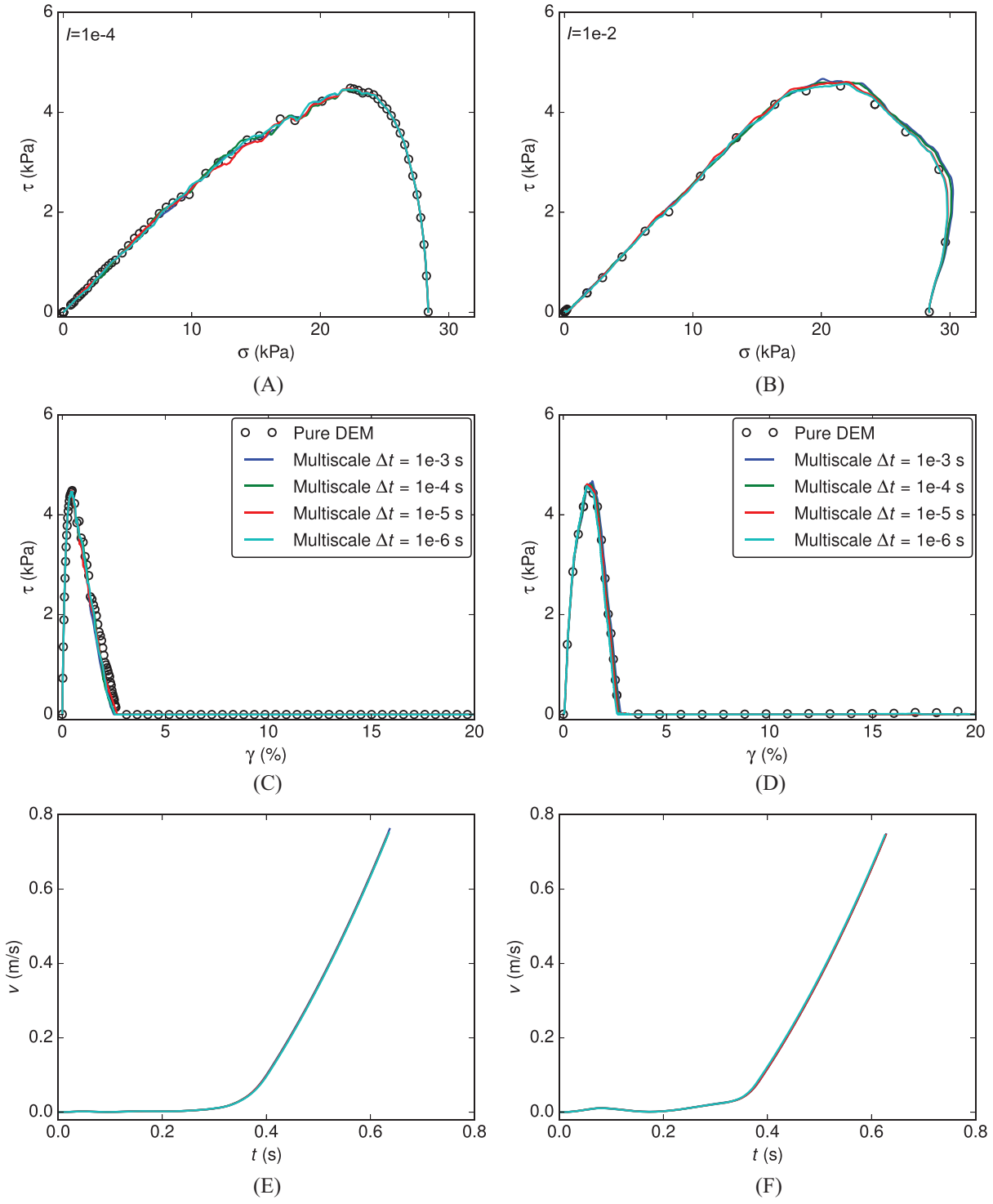

FIGURE 7 Convergence of multiscale modeling results coupling SCM with RD-DEM and comparison with pure DEM simulation response: (A) stress path, (C) stress-strain relation, and (E) sliding velocity evolution for loading rate of I = 1e-4; (B) stress path, (D) stress-strain relation, and (F) sliding velocity evolution for loading rate of I = 1e-2. DEM, discrete element method; RD-DEM, rate-dependent DEM; SCM, sliding-consolidation model.

TABLE 2 Model parameters for sliding consolidation model.

ρ_{sat} (kg/m^3)	ρ_d (kg/m^3)	h (m)	h_s (m)	k (m/s)
2000	1500	2	0.2	0

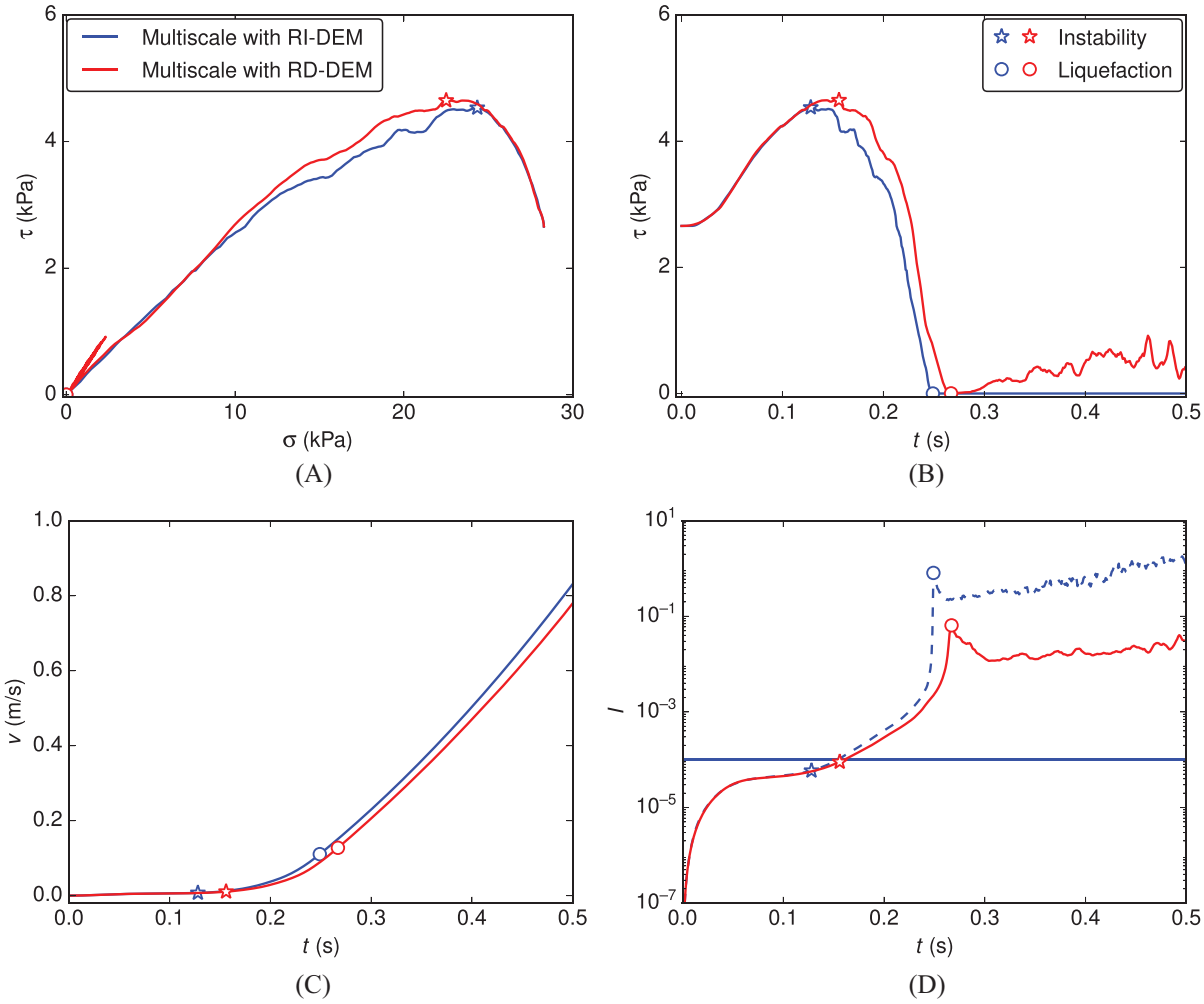

FIGURE 8 Comparison in multiscale modeling results of coupling SCM with RD-DEM versus RI-DEM for sloping ground with slope angle $\theta = 5°$: (A) stress path, and evolutions of (B) shear stress, (C) sliding velocity and (D) inertial number I where dashed line refers to the computed I using sliding velocity υ for SCM coupled with RI-DEM. DEM, discrete element method; RD-DEM; rate-dependent DEM; RI-DEM, rate-independent DEM; SCM, sliding-consolidation model.

of quasi-static loading (less than 1e-3), indicating the system's stability. Once the stress path surpasses the instability point, slight differences emerge between the two simulations, and the system starts to accelerate, resulting in drastic increase in sliding velocity. This acceleration is caused by the imbalance between the applied driving stress, τ_d, and the rapidly decreasing values of resisting stress, τ. Eventually, the system reaches a state of full liquefaction, characterized by extremely low values of normal effective stress σ and peak values of inertial number, as indicated by the circular marker. Following this state, the two simulations diverge noticeably: the shear stress τ computed by RI-DEM remains negligible, while the RD-DEM exhibits fluctuating shear stress with noticeable magnitudes, as illustrated in Figure 8B. These post-liquefaction oscillations in the shear stress of the SCM/RD-DEM simulation arise from particle agitations resulting from the high sliding velocity. These rate-dependent elevated shear stresses contribute to a higher resistance against the external stress τ_d, which in turn reduces slope acceleration and delays the development of sliding velocity, as demonstrated in Figure 8C.

Along with the shear stress oscillations, Figure 8D illustrates the variations in I within the RD-DEM sample. These variations reflect changes in the shear strain rate $\dot{\gamma}$ (or sliding velocity) and σ. While we manipulate the value of local-scale $\dot{\gamma}_L$ applied to the RI-DEM sample to maintain a constant I, the calculated I in RI-DEM using the global-scale $\dot{\gamma}_G$, as indicated by the dashed line, exhibits a higher magnitude of I compared to the RD-DEM sample. Although both multiscale simulations display a similar evolution of sliding velocity (Figure 8C), it can be concluded that higher strain rate induces larger σ values in the liquefaction regime, as demonstrated in Figure 9A, which aligns with observations in a prior study.[50] This increase in σ indicates the tendency of the RD-DEM sample to dilate, which under constant-volume conditions, effectively brings the sample out of a liquefaction regime. In contrast, the RI-DEM sample, subjected to much lower shear

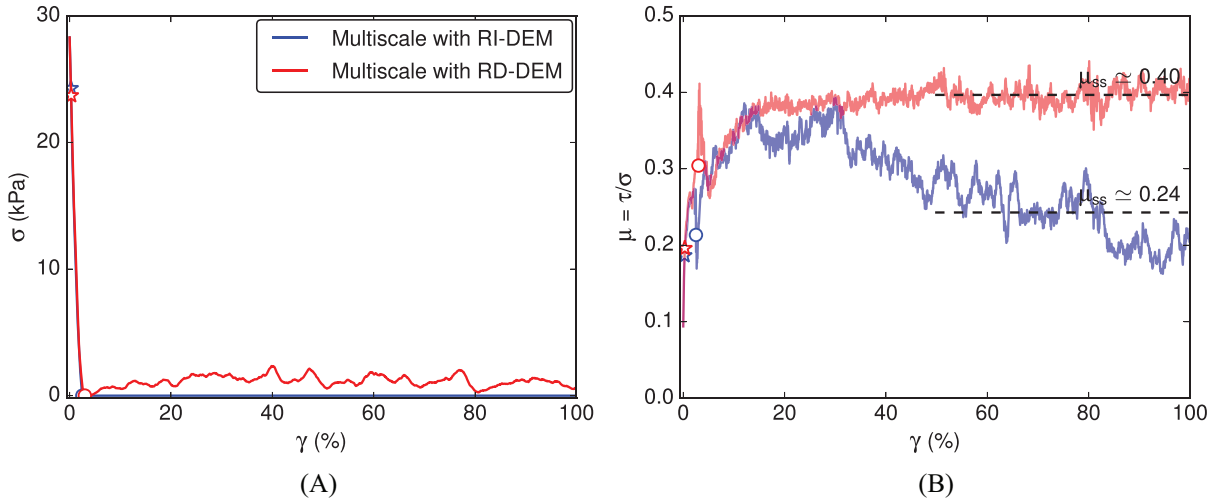

FIGURE 9 Development of (A) normal stress σ and (B) transient friction coefficient μ in multiscale simulations using constant τ_d under the sloping ground with slope angle $\theta = 5°$.

strain rate, maintains a lower σ with negligible dilation and thus remains in the liquefaction regime. As the shearing process continues, both DEM samples gradually approach a steady state characterized by vanishing volumetric response. To determine the steady state, we examine the evolution of the transient friction coefficient, defined by the stress ratio τ/σ, as shown in Figure 9B. We assume that the steady state is reached when the shear strain γ exceeds 50%. The value of μ at steady state, denoted as μ_{ss}, is determined by calculating the mean of μ values when $\gamma > 50\%$, as indicated in Figure 9B. It is worth noting that the RD-DEM sample exhibits a notably higher value of μ_{ss} compared to the RI-DEM sample. This observation aligns with the $\mu(I)$ rheology in granular flows,[5,12] where μ_{ss} increases with increasing I. In the case of the RD-DEM sample, the post-liquefaction shear stresses stem from two sources by referring to $\tau = \mu(I)\sigma$: first, the shear-induced transient dilation intensified by the large strain rate, arising from the solid-like nature of the granular system, and second, the increasing friction coefficient at steady state, contributing to the effective viscosity[12] due to the fluid-like behavior.

Figure 10 presents the distributions of shear velocity, shear stress, and vertical stress along the thickness of the DEM sample within the multiscale simulation with RD-DEM, to reveal potential non-homogeneity. In this analysis, we partition the DEM sample into 10 equal sublayers along the z axis. For each sublayer, we calculate the average shear velocity $\langle v_x \rangle$, average shear stress $\langle \tau \rangle$, and average vertical stress $\langle \sigma \rangle$. To facilitate comparisons, $\langle v_x \rangle$ is normalized by the shear velocity of the top layer $\langle v_x \rangle_{top}$. Likewise, $\langle \tau \rangle$ and $\langle \sigma \rangle$ are normalized by the homogenized counterparts, τ and σ respectively. Figure 10A demonstrates a nearly linear distribution of $\langle v_x \rangle$ along the z axis prior to soil liquefaction. However, the applicability of this linear relation deteriorates after soil liquefaction, indicating the transferring momentum downwards. As a result, the value of $\langle \tau \rangle$ in the top layers notably increases. Interestingly, this non-homogeneity is not observed for $\langle \sigma \rangle$. To mitigate this issue, one can consider implementing Lees-Edwards boundary conditions for example refs. [51, 52], to enforce the desired linear relation between $\langle v_x \rangle$ and z.

3.2 | Flowslide runout

In order to analyze the flowslide runout, we apply a transient shear stress history capable of triggering an instability[29] using a sinusoidal function: $\Delta\tau_d = A \sin(\pi t/T)$ for $t < T$. The shear pulse $\Delta\tau_d$ is then removed for $t \geq T$ to examine the resulting runout response. To replicate a small and short-lived perturbation, the amplitude A of the shear pulse is initially set to 3 kPa (the resulting stress path is provided in Figure 8A), and the duration of the pulse, T, is set to 2 s. Figure 11 compares the flow dynamics based on multiscale simulations using SCM/RD-DEM and SCM/RI-DEM for a sloping ground with an angle of $\theta = 5°$. As expected, both simulations present similar pre-liquefaction stress paths as shown in the inset in Figure 11B. The evolution of the sliding velocity in Figure 11A starts to diverge when v increases beyond 2 m/s in the post-liquefaction period. The reducing acceleration observed in the multiscale simulation with RD-DEM is attributed to the post-liquefaction elevated shear stress evolving with the dilative granular system, reflected by the

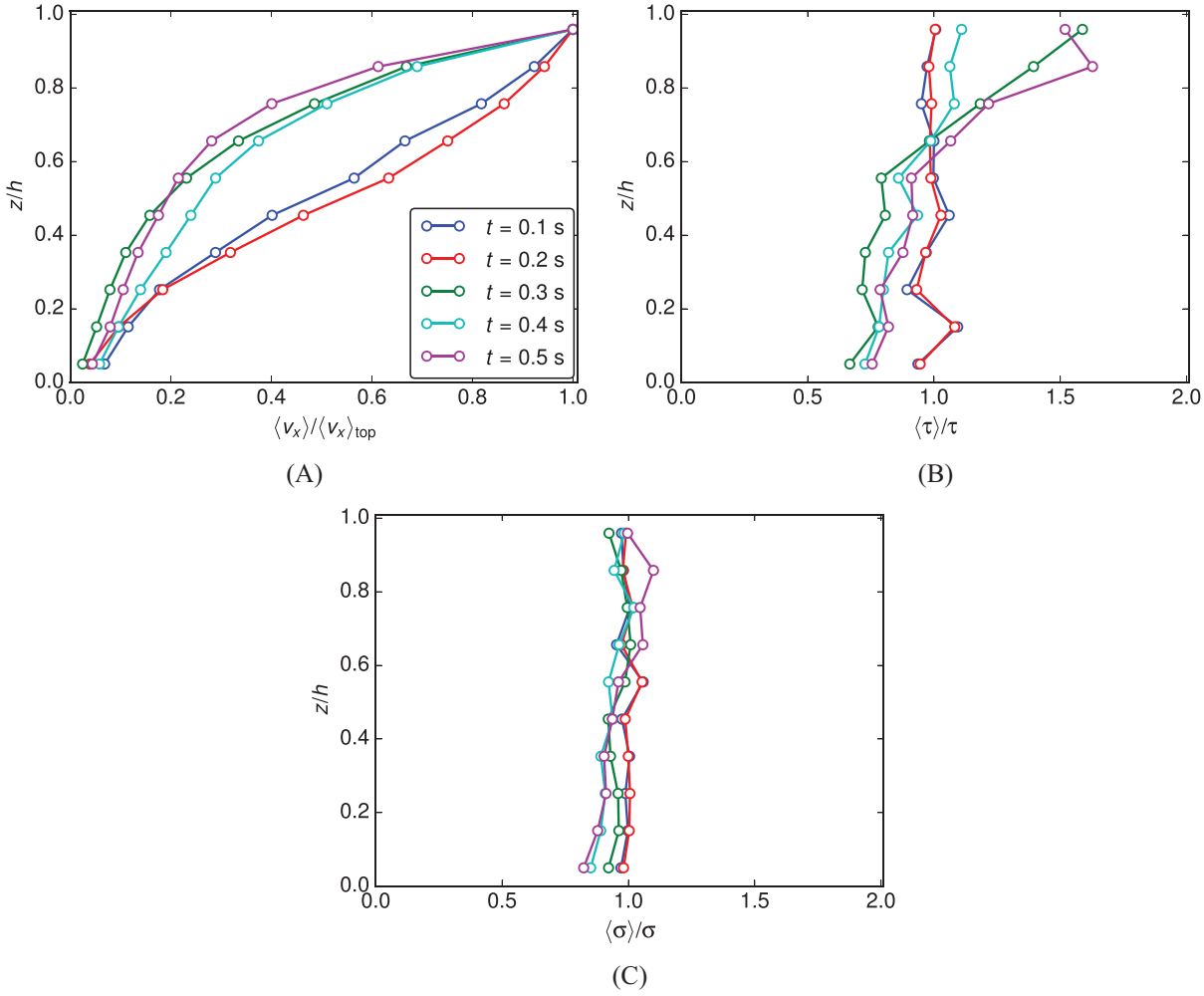

FIGURE 10 Distributions of (A) normalized average shear velocity, (B) normalized shear stress, and (C) normalized normal stress along the depth of the DEM sample at different snapshots along the multiscale simulation with RD-DEM. DEM, discrete element method; RD-DEM; rate-dependent DEM.

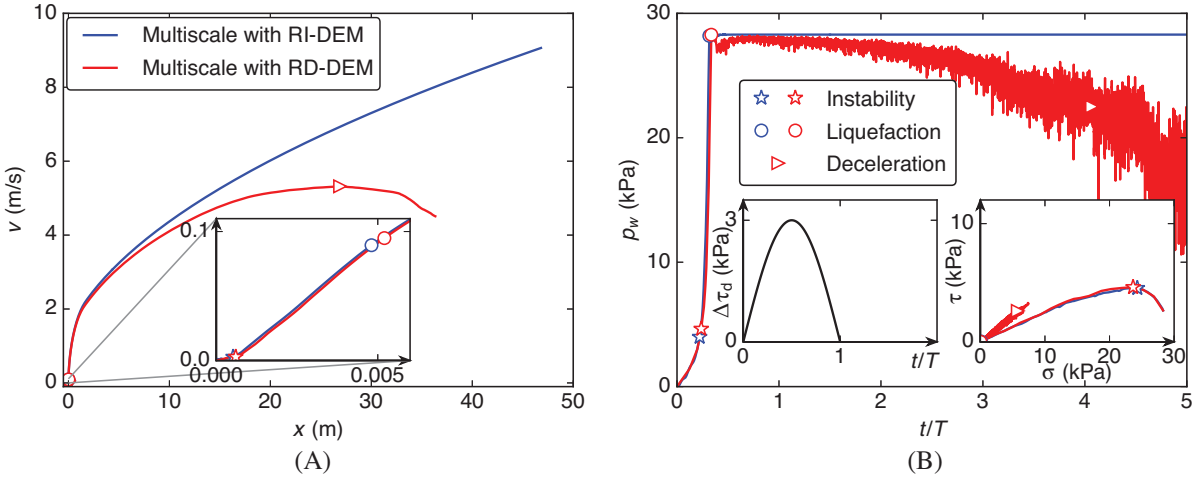

FIGURE 11 Comparison in multiscale modeling results of coupling SCM with RD-DEM versus RI-DEM for sloping ground with slope angle $\theta = 5°$: (A) flow velocity versus sliding distance and (B) pore pressure evolution. DEM, discrete element method; RD-DEM; rate-dependent DEM; RI-DEM, rate-independent DEM; SCM, sliding-consolidation model.

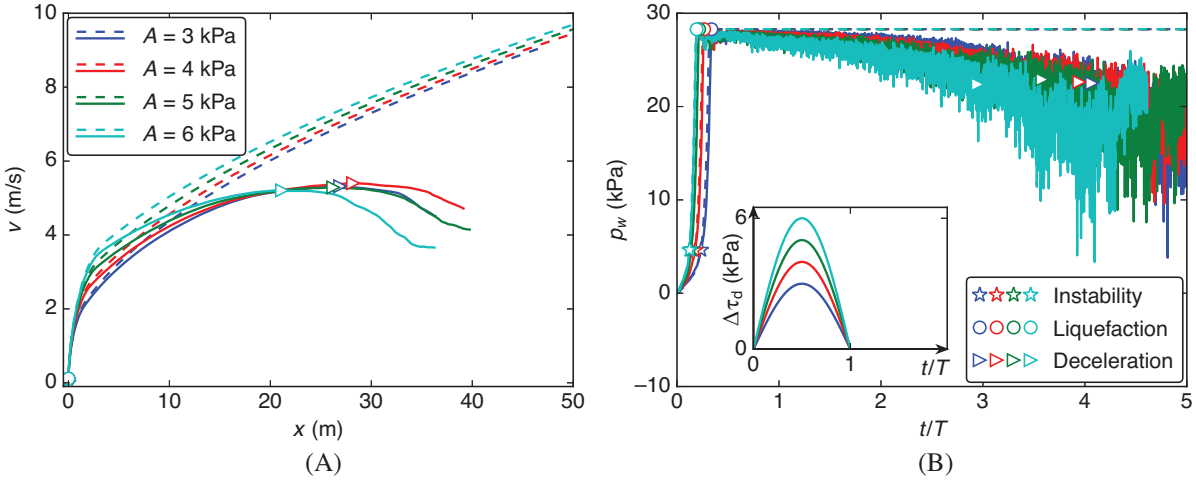

FIGURE 12 Effect of sinusoidal pulse amplitude A on the flowslide dynamics based on multiscale modeling results of coupling SCM with RD-DEM (solid line) versus RI-DEM (dashed line) for sloping ground with slope angle $\theta = 5°$: (A) flow velocity versus sliding distance and (B) pore pressure evolution. DEM, discrete element method; RD-DEM; rate-dependent DEM; RI-DEM, rate-independent DEM; SCM, sliding-consolidation model.

increasing excess pore pressure in Figure 11B. The continuously increasing sliding velocity will enhance these dynamic effects compared to the triggering analysis in Figure 8A. The magnitude of the shear stress enhanced by internal inertial effects can occasionally become larger than τ_d after the pulse, which eventually decelerates the growth of the sliding velocity. Upon further movement, the reduced flow velocity will in turn decrease the rate-dependent shear contributions below the current value of driving shear stress τ_d, thus enabling again further acceleration. This type of cycle will continue until an expected steady state with a constant sliding velocity that enables an internal shear stress balanced with τ_d.

A comparison between the post-liquefaction results obtained with RI- and RD-DEM analyses shows major differences. It is readily apparent that RI-DEM simulations predict a sand response affected by a permanent state of fully liquefaction (i.e., lack of effective stress confinement). The fully liquefied condition corresponds to a steady-state unaffected by dilative volume change fluctuations that may promote rate-dependent strengthening. Hence, after the sinusoidal pulse, the sliding velocity evolves with a constant acceleration given constant τ_d and vanishing τ, which corresponds to a parabolic relation between sliding velocity v and runout x.

RD-DEM simulations restore internal inertial feedbacks, which are in turn regulated by the characteristics of the shear pulse (i.e., its magnitude and duration). For example, Figure 12 illustrates the results obtained by varying the sinusoidal pulse amplitude A without changing the period T. The multiscale simulations conducted using RI-DEM demonstrate that increasing the sliding velocity and displacement is expected when A increases. This is because varying A does not alter the steady-state strength of the RI-DEM sample, resulting in an increase in the sliding acceleration. In the case of RD-DEM, the effect of increasing A on the simulation results is evident before reaching the deceleration point. Prior to this point, the DEM sample has not regained sufficient shear strength to balance the post-pulse external loading. However, as the strain rate increases, the DEM sample eventually acquires significant shear strength. Consequently, the paths of v and x start to converge, irrespective of A, revealing a consistent v_{max}. This convergence of paths implies that the RD-DEM sample loses memory of its previous loading history and exhibits more fluid-like behavior.

The choice of $k = 0$ m/s in the simulations suppresses the mechanism of excess pore pressure dissipation. However, in Figure 13, this constraint is removed, and five different small values of hydraulic conductivity are introduced to ensure instability triggering. The effect of hydraulic conductivity on the flowslide runout in the multiscale SCM/RD-DEM simulations is noticeable. Increasing k leads to a decrease in the maximum sliding velocity and the corresponding runout. This can be attributed to the enhanced dilative tendency, as indicated by the earlier increase in pore pressure in Figure 13B. However, it is important to note that this observation does not fully apply to the multiscale SCM/RI-DEM simulations where the non-zero hydraulic conductivity provides the sole source of dissipating excess pore pressure. In this case, a critical value of hydraulic conductivity is required to sufficiently balance the contraction tendency of the RI-DEM sample, thereby bringing its steady state out of the liquefaction regime. Base on Figure 13A, this critical value is approximately

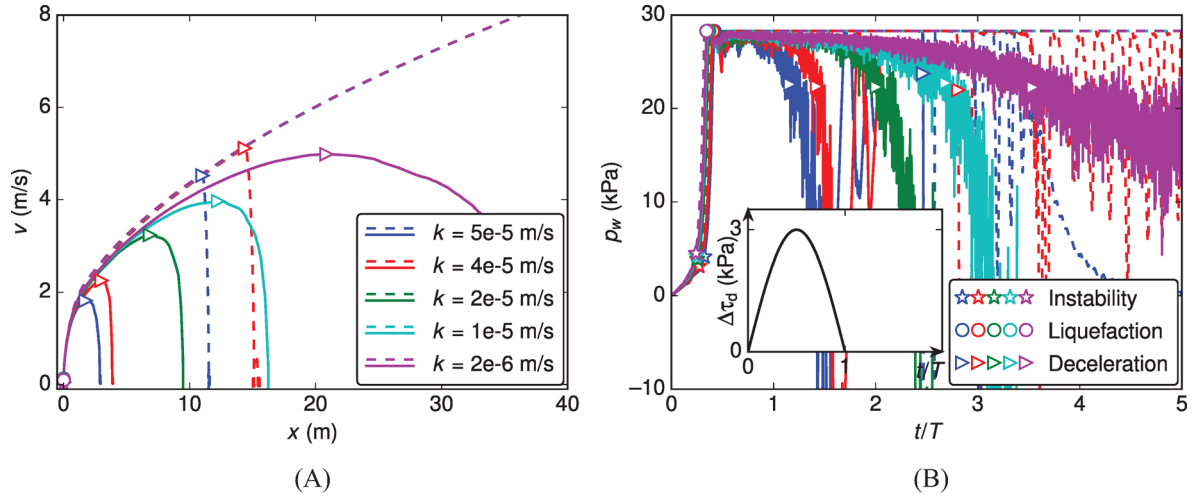

FIGURE 13 Effect of hydraulic conductivity k on the flowslide dynamics based on multiscale modeling results of coupling SCM with RD-DEM (solid line) versus RI-DEM (dashed line) for sloping ground with slope angle $\theta = 5°$: (A) flow velocity versus sliding distance and (B) pore pressure evolution. DEM, discrete element method; RD-DEM; rate-dependent DEM; RI-DEM, rate-independent DEM; SCM, sliding-consolidation model.

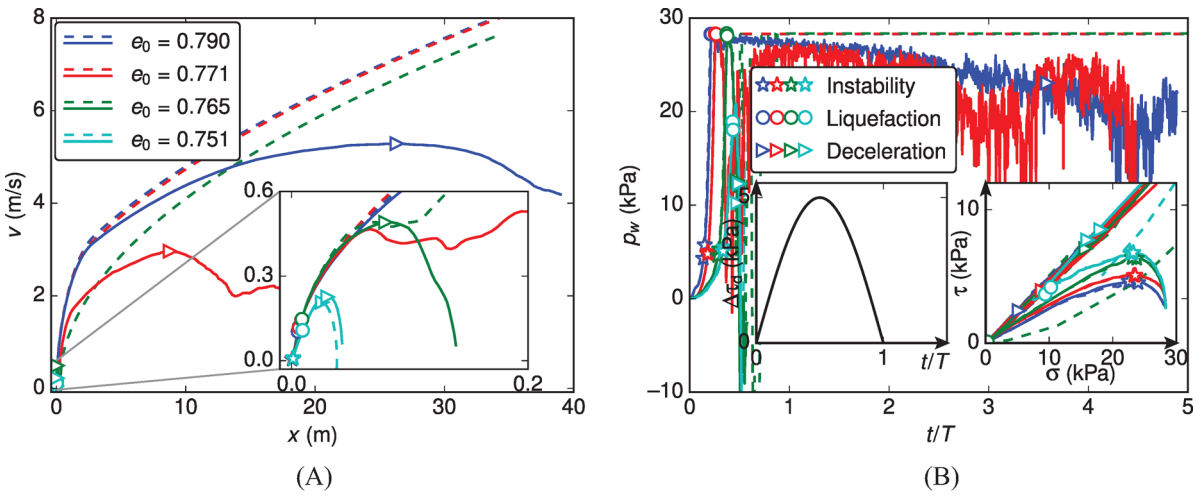

FIGURE 14 Effect of DEM sample initial void ratio e_0 on the flowslide dynamics based on multiscale modeling results of coupling SCM with RD-DEM (solid line) versus RI-DEM (dashed line) for sloping ground with slope angle $\theta = 5°$: (A) flow velocity versus sliding distance and (B) pore pressure evolution. DEM, discrete element method; RD-DEM; rate-dependent DEM; RI-DEM, rate-independent DEM; SCM, sliding-consolidation model.

4e-5 m/s. Once the hydraulic conductivity exceeds this critical value, we observe a similar effect of k on the flowslide runout in the multiscale simulations with RI-DEM.

In addition to varying hydraulic conductivity to facilitate excess pore pressure dissipation, another approach to reduce the velocity of flowslide motion is to increase the density of the DEM sample, which enhances its dilative tendency. Figure 14 illustrates the multiscale simulation results of four loose DEM samples, whose macroscopic response under quasi-static loading is shown in Figure 3. The DEM sample with $e_0 = 0.771$ exhibits noticeable post-liquefaction shear stress fluctuations in the constant-volume simple shear test in Figure 3B. However, in the multiscale simulation with RI-DEM, its fragile contact network does not affect the sliding velocity evolution. When incorporating the rate-dependency through RD-DEM, the corresponding multiscale simulation result is astonishing, showing much smaller sliding velocity and displacement, compared to the very loose sample with $e_0 = 0.790$. The effect of volume dilation becomes significant in the multiscale simulation with RI-DEM when considering the sample with $e_0 = 0.765$, where the rate-dependent nature still introduces much difference in the simulated macroscopic response. The difference in multiscale modeling using RI-

DEM versus RD-DEM becomes negligible when further reducing the sample void ratio to 0.751, as the sliding velocity becomes very small. However, this does not mean that rate-dependent effect on these samples is not significant, as the current loading pulse does not result in large sliding velocity or strain rate. If these samples were subjected to shearing under a large strain rate (such as by increasing the pulse amplitude and period), it is expected that these two types of multiscale simulations would yield distinct results. However, the difference may not be as significant as in the case of the very loose sample with $e_0 = 0.790$ due to the strong dilative tendency in these other samples.

4 | CONCLUSIONS

In this paper we propose a hierarchical multiscale modeling framework to simulate flowslide triggering and runout. This framework couples a global-scale SCM that accounts for hydro-mechanical feedbacks within a liquefied sand layer with a local-scale solver based on the DEM. This coupling is meant to seamlessly simulate the transition from solid- to fluid-like behavior following liquefaction, which is controlled by the local grain-scale dynamics. The DEM particle assembly serves as the constitutive law for the global-scale SCM, used to predict the emergent rate-dependent response of the sand during the inertial regime of motion. Unlike other multiscale modeling methods that presume a rate-independent nature for the local DEM sample, this approach incorporates both strain increment and strain rate in the passage of information from the global to the local scale.

We first investigate the effect of the loading rate on the stress tensor calculation of the DEM sample and find that it has a negligible influence, confirming the choice of using Bagi's stress tensor in this study. Next, we address a numerical issue encountered when transitioning from quasi-static loading in the local-scale DEM solver to dynamic loading, that is, how to ensure the correct passage of the strain rate from the global analysis to the local DEM solver. A numerical strategy is proposed in this study by accumulating the local strain increment until a sufficient amount is reached, so that the DEM sample can be sheared under the desired strain rate, resolving the bottleneck that possibly hinders the dynamic analysis. This novel algorithm enables the incorporation of the actual strain rate emerging from global balance equations, eliminating the need of rescaling the local timescale of computation for DEM analyses. We adopt explicit time integration scheme to numerically integrate the governing equations of the global-scale SCM and the multiscale modeling framework supports parallel computing using MPI.

Using this multiscale modeling framework, we simulate flowslide triggering and runout based on loose DEM samples. At the local scale, we introduce two modes, rate-dependent DEM (RD-DEM) and rate-independent DEM (RI-DEM), depending on whether the global-scale strain rate is used to shear the DEM sample. By comparing the multiscale simulation results of RD-DEM versus RI-DEM, we observe no noticeable difference in the grain-scale dynamics during the triggering process. However, we do observe significant effects of micro-inertial feedback on the runout, where post-liquefaction particle agitation generates spontaneous viscous-like effects that ultimately slow down the flowslide propagation. In the analysis of varying flowslide triggering magnitudes, we confirm that the sample exhibiting micro-inertial effects loses memory of its previous loading history. Additionally, we observe that facilitating pore pressure diffusion and enhancing the dilative tendency of the samples contribute to slowing down the flowslide movement.

It is important to note that this study primarily addresses the computational challenges inherent in multiscale modeling, particularly when dealing with dynamic systems. However, open issues still remain regarding the synchronization of global- and local-scale dynamic systems throughout the loading process. In particular, further research is needed with reference to the interplay between the natural frequency of the multiple dynamic systems involved in the analysis. Additionally, the simple assumption of equally transferring the global-scale strain rate to the local scale warrants further investigation, possibly by providing theoretical support for this transfer from the perspective of energy conservation. Despite these open questions, extending the current study by replacing the global-scale SCM with a more versatile solver capable of simulating large deformations, such as MPM and SPH, would be a valuable endeavor. This extension could facilitate exploring the impact of strain rate on the classic dynamic problems, such as soil column collapse, laboratory flume test, and full-scale analyses of flowslide events.

ACKNOWLEDGMENTS

This work was partially supported by the US National Science Foundation through grant ICER-1854951. Acknowledgment is also given to the donors of the American Chemical Society Petroleum Research Fund for partial support of this research. The authors are also grateful for the additional support provided by Leslie and Mac McQuown, as well as to Dr Jidong Zhao

and Dr Petia Vlahovska for the useful feedback provided during the conduction of this study. The authors express gratitude to the Texas Advanced Computing Center (TACC) at The University of Texas at Austin for providing HPC resources that have contributed to the research results reported within this paper.

DATA AVAILABILITY STATEMENT

Data from the numerical analyses discussed in this paper can be made available to interested readers upon direct request to the authors.

ORCID

Ming Yang https://orcid.org/0000-0002-6409-3942
Giuseppe Buscarnera https://orcid.org/0000-0003-1664-9616

REFERENCES

1. Wartman J, Montgomery DR, Anderson SA, et al. The 22 March 2014 Oso landslide, Washington, USA. *Geomorphology*. 2016;253:275-288. doi:10.1016/j.geomorph.2015.10.022
2. Santamarina JC, Torres-Cruz LA, Bachus RC. Why coal ash and tailings dam disasters occur. *Science*. 2019;364 (6440):526-528. doi:10.1126/science.aax1927
3. Rotta LHS, Alcântara E, Park E, et al. The 2019 Brumadinho tailings dam collapse: possible cause and impacts of the worst human and environmental disaster in Brazil. *Int J Appl Earth Obs Geoinf*. 2020;90:102119. doi:10.1016/j.jag.2020.102119
4. Pradel D, Lobbestael A, Brooks CN, et al. *The May 19, 2020, Failure of Edenville Dam near Midland, Michigan*. American Society of Civil Engineers; 2021:266-274.
5. Cruz dF, Emam S, Prochnow M, Roux JN, Chevoir F. Rheophysics of dense granular materials: discrete simulation of plane shear flows. *Phys Rev E*. 2005;72 (2):021309. doi:10.1103/PhysRevE.72.021309
6. Seyedan S, Sołowski WT. From solid to disconnected state and back: continuum modelling of granular flows using material point method. *Comput Struct*. 2021;251:106545. doi:10.1016/j.compstruc.2021.106545
7. Dafalias YF. Bounding surface plasticity. I: mathematical foundation and hypoplasticity. *J Eng Mech*. 1986;112 (9):966-987. doi:10.1061/(ASCE)0733-9399(1986)112:9(966)
8. Jefferies MG. Nor-Sand: a simle critical state model for sand. *Géotechnique*. 1993;43 (1):91-103. doi:10.1680/geot.1993.43.1.91
9. Gajo A, Wood DM. A kinematic hardening constitutive model for sands: the multiaxial formulation. *Int J Numer Anal Methods Geomech*. 1999;23 (9):925-965. doi:10.1002/(SICI)1096-9853(19990810)23:9⟨925::AID-NAG19⟩3.0.CO;2-M
10. Taiebat M, Dafalias YF. SANISAND: Simple anisotropic sand plasticity model. *Int J Numer Anal Methods Geomech*. 2008;32 (8):915-948. doi:10.1002/nag.651
11. Yang M, Taiebat M, Dafalias YF. SANISAND-MSf: a sand plasticity model with memory surface and semifluidised state. *Géotechnique*. 2022;72 (3):227-246. doi:10.1680/jgeot.19.p.363
12. Jop P, Forterre Y, Pouliquen O. A constitutive law for dense granular flows. *Nature*. 2006;441 (7094):727-730. doi:10.1038/nature04801
13. Goldhirsch I. Rapid granular flows. *Annu Rev Fluid Mech*. 2003;35 (1):267-293. doi:10.1146/annurev.fluid.35.101101.161114
14. Dunatunga S, Kamrin K. Continuum modelling and simulation of granular flows through their many phases. *J Fluid Mech*. 2015;779:483-513. doi:10.1017/jfm.2015.383
15. Redaelli I, Ceccato F, Prisco dC, Simonini P. Solid-fluid transition in granular flows: MPM simulations with a new constitutive approach. *Procedia Eng*. 2017;175:80-85. doi:10.1016/j.proeng.2017.01.028
16. Alaei E, Marks B, Einav I. A hydrodynamic-plastic formulation for modelling sand using a minimal set of parameters. *J Mech Phys Solids*. 2021;151:104388. doi:10.1016/0266-352X(96)00005-5
17. Marveggio P, Redaelli I, Prisco dC. Phase transition in monodisperse granular materials: how to model it by using a strain hardening visco-elastic-plastic constitutive relationship. *Int J Numer Anal Methods Geomech*. 2022;46 (13):2415-2445. doi:10.1002/nag.3412
18. Fish J, Wagner GJ, Keten S. Mesoscopic and multiscale modelling in materials. *Nat Mater*. 2021;20 (6):774-786. doi:10.1038/s41563-020-00913-0
19. Miehe C, Dettmar J, Zäh D. Homogenization and two-scale simulations of granular materials for different microstructural constraints. *Int J Numer Methods Eng*. 2010;83 (8-9):1206-1236. doi:10.1002/nme.2875
20. Guo N, Zhao J. A coupled FEM/DEM approach for hierarchical multiscale modelling of granular media. *Int J Numer Methods Eng*. 2014;99 (11):789-818. doi:10.1002/nme.4702
21. Liu Y, Sun W, Yuan Z, Fish J. A nonlocal multiscale discrete-continuum model for predicting mechanical behavior of granular materials. *Int J Numer Methods Eng*. 2015;106 (2):129-160. doi:10.1002/nme.5139
22. Shahin G, Desrues J, Pont SD, Combe G, Argilaga A. A study of the influence of REV variability in double-scale FEM × DEM analysis. *Int J Numer Methods Eng*. 2016;107:882-900. doi:10.1002/nme.5202
23. Liang W, Zhao J. Multiscale modeling of large deformation in geomechanics. *Int J Numer Anal Methods Geomech*. 2019;43 (5):1080-1114. doi:10.1002/nag.2921
24. Guo N, Yang Z, Yuan W, Zhao J. A coupled SPFEM/DEM approach for multiscale modeling of large-deformation geomechanical problems. *Int J Numer Anal Methods Geomech*. 2021;45 (5):648-667. doi:10.1002/nag.3175

25. Liang W, Zhao J, Wu H, Soga K. Multiscale, multiphysics modeling of saturated granular materials in large deformation. *Comput Meth Appl Mech Eng*. 2023;405:115871. doi:10.1016/j.cma.2022.115871
26. Chan AH, Pastor M, Schrefler BA, Shiomi T, Zienkiewicz OC. *Computational Geomechancis: Theory and Application*. John Wiley & Sons; 2022.
27. Hutchinson JN. A sliding–consolidation model for flow slides. *Can Geotech J*. 1986;23 (2):115-126. doi:10.1139/t86-021
28. Iverson RM. Regulation of landslide motion by dilatancy and pore pressure feedback. *J Geophys Res Earth Surf*. 2005;110(F02015). doi:10.1029/2004JF000268
29. Chen Y, Buscarnera G. Unified modeling framework of flowslide triggering and runout. *Géotechnique*. 2022. doi:10.1680/jgeot.21.00370
30. Li X, Chen Y, Handwerger AL, Buscarnera G. Dynamics of creeping landslides controlled by inelastic hydro-mechanical couplings. *Eng Geol*. 2023;317:107078. doi:10.1016/j.enggeo.2023.107078
31. Li X, Handwerger AL, Buscarnera G. Viscoplastic modelling of rainfall-driven slow-moving landslides: application to California Coast Ranges. *Landslides*. 2023;20 (6):1101-1113. doi:10.1007/s10346-023-02039-1
32. Kloss C, Goniva C, Hager A, Amberger S, Pirker S. Models, algorithms and validation for opensource DEM and CFD–DEM. *Prog Comput Fluid Dyn, Int J*. 2012;12 (2-3):140-152. doi:10.1504/PCFD.2012.047457
33. Ai J, Chen JF, Rotter JM, Ooi JY. Assessment of rolling resistance models in discrete element simulations. *Powder Technol*. 2011;206 (3):269-282. doi:10.1016/j.powtec.2010.09.030
34. Cavarretta I, Coop M, O'Sullivan C. The influence of particle characteristics on the behaviour of coarse grained soils. *Géotechnique*. 2010;60 (6):413-423. doi:10.1680/geot.2010.60.6.413
35. Balamonica K, Goh SH. Characterisation of contact parameters of sand grains to be used for discrete element modelling. *E3S Web Conf*. 2019;92:14002. doi:10.1051/e3sconf/20199214002
36. Guo N, Zhao J. The signature of shear-induced anisotropy in granular media. *Comput Geotech*. 2013;47:1-15. doi:10.1016/j.compgeo.2012.07.002
37. Yang M, Taiebat M, Mutabaruka P, Radjaï F. Evolution of granular materials under isochoric cyclic simple shearing. *Phys Rev E*. 2021;103:032904. doi:10.1103/PhysRevE.103.032904
38. Yang M, Taiebat M, Mutabaruka P, Radjaï F. Evolution of granular media under constant-volume multidirectional cyclic shearing. *Acta Geotech*. 2021;17:779-802. doi:10.1007/s11440-021-01239-0
39. O'Sullivan C. *Particulate Discrete Element Modelling: A Geomechanics Perspective*. CRC Press; 2011
40. Kuhn MR. *Granular Geomechanics*. Elsevier; 2017.
41. Nicot F, Hadda N, Guessasma M, Fortin J, Millet O. On the definition of the stress tensor in granular media. *Int J Solids Struct*. 2013;50 (14-15):2508-2517. doi:10.1016/j.ijsolstr.2013.04.001
42. Bagi K. Stress and strain in granular assemblies. *Mech Mater*. 1996;22 (3):165-177. doi:10.1016/0167-6636(95)00044-5
43. Weber J. Recherches concernant les contraintes intergranulaires dans les milieux pulvérulents. *Bulletin de liaison des Ponts et Chaussées*. 1966;20:1-20.
44. Christoffersen J, Mehrabadi MM, Nemat-Nasser S. A micromechanical description of granular material behavior. *J Appl Mech*. 1981;48 (2):339-344. doi:10.1115/1.3157619
45. Yan B, Regueiro RA. Definition and symmetry of averaged stress tensor in granular media and its 3D DEM inspection under static and dynamic conditions. *Int J Solids Struct*. 2019;161:243-266. doi:10.1016/j.ijsolstr.2018.11.021
46. Yang M. *Micro-and macromechanical modeling of granular materials under constant volume cyclic shearing*. PhD thesis. The University of British Columbia; 2020.
47. Weinhart T, Hartkamp R, Thornton AR, Luding S. Coarse-grained local and objective continuum description of three-dimensional granular flows down an inclined surface. *Phys Fluids*. 2013;25(7):070605. doi:10.1063/1.4812809
48. Martin EL, Thornton C, Utili S. Micromechanical investigation of liquefaction of granular media by cyclic 3D DEM tests. *Géotechnique*. 2020;70 (10):906-915. doi:10.1680/jgeot.18.p.267
49. Kuhn MR. Multi-scale simulation of wave propagation and liquefaction in a one-dimensional soil column: hybrid DEM and finite-difference procedure. *Acta Geotech*. 2021;17 (7):2611-2632. doi:10.1007/s11440-021-01402-7
50. Yang M, Taiebat M, Radjaï F. Liquefaction of granular materials in constant-volume cyclic shearing: transition between solid-like and fluid-like states. *Comput Geotech*. 2022;148:104800. doi:10.1016/j.compgeo.2022.104800
51. Lees AW, Edwards SF. The computer study of transport processes underextreme conditions. *J Phys C: Solid State Phys*. 1972;5:1921.
52. Berry N, Zhang Y, Haeri S. Lees-Edwards boundary conditions for the multi-sphere discrete element method. *Powder Technol*. 2021;389:292-308. doi:10.1016/j.powtec.2021.05.025

How to cite this article: Yang M, Buscarnera G. Multiscale modeling of granular dynamics on flowslide triggering and runout. *Int J Numer Anal Methods Geomech*. 2024;48:1720–1739. https://doi.org/10.1002/nag.3705